

Virtual and Physical Prototyping

ISSN: (Print) (Online) Journal homepage: <https://www.tandfonline.com/loi/nvpp20>

Robot-assisted conformal additive manufacturing for continuous fibre-reinforced grid-stiffened shell structures

Guoquan Zhang, Yaohui Wang, Ziwen Chen, Xuguang Xu, Ke Dong & Yi Xiong

To cite this article: Guoquan Zhang, Yaohui Wang, Ziwen Chen, Xuguang Xu, Ke Dong & Yi Xiong (2023) Robot-assisted conformal additive manufacturing for continuous fibre-reinforced grid-stiffened shell structures, *Virtual and Physical Prototyping*, 18:1, e2203695, DOI: [10.1080/17452759.2023.2203695](https://doi.org/10.1080/17452759.2023.2203695)

To link to this article: <https://doi.org/10.1080/17452759.2023.2203695>



© 2023 The Author(s). Published by Informa UK Limited, trading as Taylor & Francis Group



Published online: 04 May 2023.



Submit your article to this journal



Article views: 18



View related articles



View Crossmark data

CrossMark

Robot-assisted conformal additive manufacturing for continuous fibre-reinforced grid-stiffened shell structures

Guoquan Zhang^a, Yaohui Wang^a, Ziwen Chen^a, Xuguang Xu^a, Ke Dong^b and Yi Xiong   ^a

^aSchool of System Design and Intelligent Manufacturing, Southern University of Science and Technology, Shenzhen, Guangdong, People's Republic of China; ^bDepartment of Industrial and Systems Engineering, The Hong Kong Polytechnic University, Kowloon, Hong Kong

ABSTRACT

The advents in continuous fibre-reinforced polymer additive manufacturing (CFRP-AM) present unprecedented opportunities for the rapid development of next-generation high-performance composites with selectively and spatially distributed reinforcement. However, the widely adopted 3-degree-of-freedom motion configuration in current CFRP-AM systems hinders the exploration of composite structures with non-planar fibre layouts. This work presents a novel conformal CFRP-AM system to fabricate grid-stiffened shell structures leveraging its multi-DoF motion to pattern spatial features. The system integrates a 6-axis robot with an optimally designed co-extrusion module and operates through a design-to-manufacturing workflow. The proposed workflow includes three steps: system calibration, conformal toolpath generation, and process implementation. The conformal toolpath generation is a surface-mapping-based method that allows a simultaneous exploration of various geometric designs and their toolpaths. Experimental comparisons were made between parts fabricated by different processes, i.e., planar and conformal based, with different toolpaths, i.e., shells filled with zigzag and arc-offset patterns, and with various geometric designs, i.e., stiffener ribs with different crossline angles. The results manifest that the proposed system can significantly improve the compression strength and stiffness of grid-stiffened shell structures. Meanwhile, the additional design freedom on process and structure opens up a new possibility to customise their mechanical performance.

ARTICLE HISTORY

Received 4 February 2023

Accepted 12 April 2023

KEYWORDS

Robotic system; grid-stiffened shell structure; continuous fibre-reinforced polymer additive manufacturing; surface conformal toolpath

1. Introduction

The shift of additive manufacturing (AM) from a prototyping technique towards a viable production option calls for advancement in its ability to fabricate engineering structures with high-performance materials (Chen et al. 2022; Suzuki, Fukushige, and Tsunori 2020; Alhijaily, Kilic, and Paulo Bartolo 2023). In this context, recent studies have focused on continuous fibre-reinforced polymer additive manufacturing (CFRP-AM), featuring its excellent ability in mechanical enhancement via selectively and spatially distributed continuous fibre reinforcement within the polymer matrix (Wang et al. 2022; Liu, Xiong, and Zhou 2021; Zhang et al. 2023; Goh et al. 2022). The composite parts have much higher specific strength and stiffness along the fibre direction than parts made with polymers alone while remaining lightweight (Sieberer et al. 2022; Bhatt et al. 2020; Hou et al. 2020). At present, various types of CFRP-AM processes have been developed, such as

laser-assisted tape placement (LATP) (Parandoush et al. 2017), laminated object manufacturing (LOM) (Bhatt et al. 2019), and material extrusion (MEX) (Matsuzaki et al. 2016; Billah et al. 2020; Kubalak, Wicks, and Williams 2018). In comparison, the MEX has gained the most widespread attention due to its lower cost and better controllability on fibre layouts (Dickson et al. 2017; van de Werken et al. 2021). Current MEX-based CFRP-AM systems are mainly developed by modifying the 3-degree-of-freedom (DoF) fused deposition molding (FDM) machine (Qiao, Li, and Li 2019; Naranjo-Lozada et al. 2019). As shown in Figure 1(a), the polymer filaments are fed into a melting chamber together with dry or pre-impregnated continuous fibres and then co-extruded onto a planar-built platform or deposited layers (Zhang et al. 2022). Within another widely used process, continuous fibres pre-impregnated with thermoplastic matrix material are heated through a melting chamber and extruded. However, the types of

CONTACT Yi Xiong  xiongy3@sustech.edu.cn  School of System Design and Intelligent Manufacturing, Southern University of Science and Technology, Shenzhen 518055, Guangdong, People's Republic of China

© 2023 The Author(s). Published by Informa UK Limited, trading as Taylor & Francis Group

This is an Open Access article distributed under the terms of the Creative Commons Attribution License (<http://creativecommons.org/licenses/by/4.0/>), which permits unrestricted use, distribution, and reproduction in any medium, provided the original work is properly cited. The terms on which this article has been published allow the posting of the Accepted Manuscript in a repository by the author(s) or with their consent.

fibre-reinforced composites that can be produced are limited, typically to Nylon. In contrast, the co-extrusion process allows the use of multiple polymer matrix materials (Zhang et al. 2022; Goh et al. 2018). In addition, the parts fabricated by the two processes exhibit close mechanical properties (Parker et al. 2022). Therefore, this study focuses on the co-extrusion process.

However, these 3-DoF motion configuration-based CFRP-AM machines are unsuitable for fabricating composite structures with non-planar fibre layouts. One example is the grid-stiffened shell structure, as illustrated in Figure 1(b), which is a class of advanced engineering structures widely used in maritime, aerospace, and architecture industries due to their high load-bearing capacity and lightweight design (Nuh et al. 2022; Vasiliev, Barynin, and Razin 2012). This structure consists of a thin-walled shell and stiffened ribs, in which the shell is often developable surface-based (Cui et al. 2017; Jiang et al. 2020); meanwhile, the ribs distributed on the shell surfaces have a grid-based layout (Nuh et al. 2022; Totaro et al. 2021). As depicted in Figure 1(b), the 3-DoF-based CFRP-AM workflow slices these non-planar shells and ribs into discrete planar layers, making it impossible to lay fibres along curved surfaces. As a result, the potential to use CFRP for enhancing interlayer mechanical properties is not realised yet (Xu et al. 2019;

Zeng et al. 2021; van de Werken et al. 2020). The weak interlayer strength of parts fabricated by 3-DoF-based machines greatly hinders the efforts to transfer CFRP-AM into a viable production option (Zhao and Guo 2020).

The emergence of multi-axis AM has shed light on the above challenge. As shown in Figure 1(d), the conformal CFRP-AM process can directly pattern non-planar features of the grid-stiffened shell structure using multi-DoF motion. Recently, such systems have been reported by several research groups (Fang et al. 2020; Nault, Ferguson, and Nardi 2021; Jiang, Xu, and Stringer 2019) and machine manufacturers, e.g. Ansioprint. However, most of these studies are limited to proof-of-concept demonstration and have only addressed hardware integration-related challenges, such as extrusion speed matching (Gibson et al. 2022; Badarinath and Prabhu 2021). The performance improvement of fabricated parts by the conformal CFRP-AM process is rarely reported. Moreover, the multi-DoF motion allows the toolpaths to be set along any desired direction rather than being limited to two dimensions to strengthen the model (Pedersen et al. 2016; Kubalak, Wicks, and Williams 2018). Therefore, generating desired conformal toolpaths becomes another great challenge for the development of CFRP-AM. Several related studies, although not for CFRP, have been conducted for generating freeform

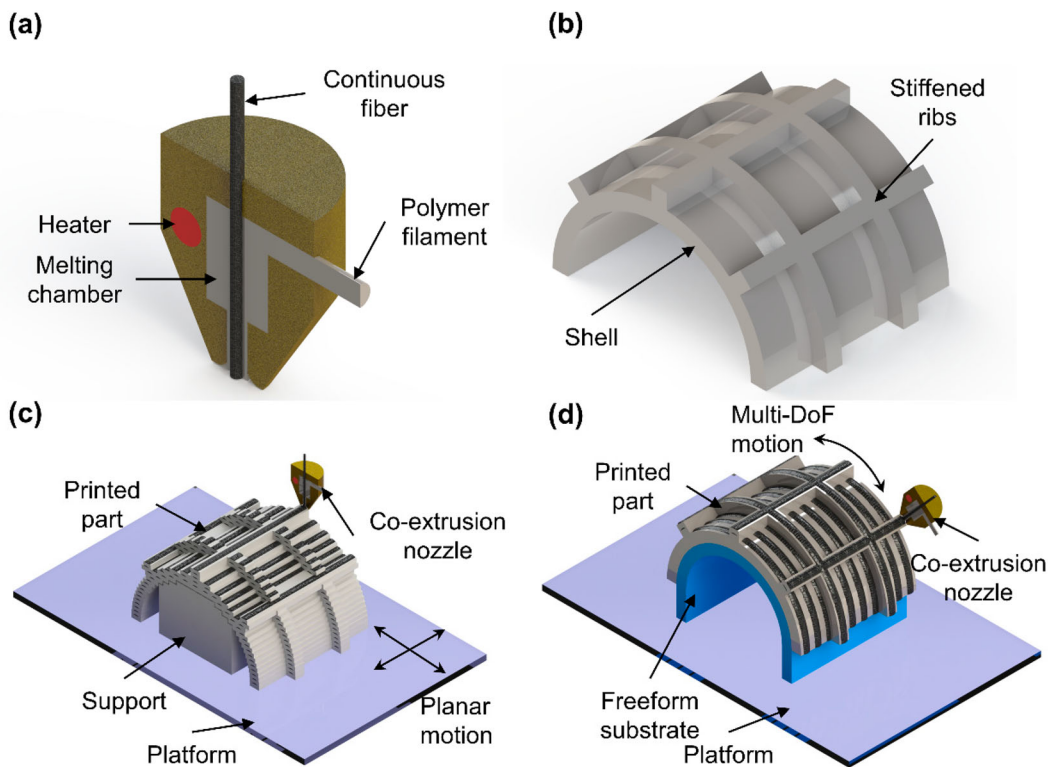


Figure 1. The CFRP-AM process for grid-stiffened shell structure: (a) the fibre-polymer co-extrusion nozzle; (b) a typical grid-stiffened shell structure; (c) 3-DoF CFRP-AM; and (d) conformal CFRP-AM.

surface toolpaths, including two main categories. Some methods aim at projecting two-dimensional (2D) hatching patterns onto three-dimensional (3D) surfaces (Alkadi et al. 2020; Shembekar et al. 2019). The 2D hatching patterns are usually iso-parametric, with equal distances between multi-beads. However, the geodesic distance between multiple beads at different locations is variable after projection onto 3D surfaces. This variation of bead-to-bead distance is incompatible with the existing constant bead width-based AM process which can lead to printing defects such as gaps and material buildup (Bi, Xie, and Tang 2021; Tan et al. 2020). Varying single bead width requires symmetrical variation about both sides of the path and is usually inefficient (Xiong et al. 2019; Zolfagharian et al. 2020). In addition, other studies (Liang, Kang, and Fang 2020; Xu et al. 2019) utilise level-set methods to generate equidistant 3D toolpaths based on the surface geodesic distance. However, this method has downsides: the generated path type is limited to contour offset types, and the computational cost is expensive. In summary, there is a lack of systematic exploration of the design-to-manufacturing workflow for the conformal CFRP-AM system. In particular, there is a lack of conformal toolpath generation methods in the workflow that can meet multi requirements simultaneously.

This work aims to advance the robot-assisted conformal CFRP-AM process for fabricating grid-stiffened shell structures. The main contributions are threefold, including manufacturing system development, conformal toolpath planning, and performance testing. First, a 6-axis robot was retrofitted with a co-extrusion module to serve as a conformal CFRP-AM system and operated through a design-to-manufacturing workflow consisting of three steps: system calibration, conformal toolpath generation, and process implementation. Second, a surface mapping-based toolpath generation method is proposed for conformal CFRP-AM processes targeting developable surfaces. This method allows a simultaneous exploration of various geometric designs (shells and ribs) and their toolpaths. The end-to-end workflow directly outputs converted machine code. Third, grid-stiffened conical shell structures with different conformal toolpaths were fabricated to verify the effectiveness of the proposed system and workflow. The compression experiments show that the mechanical properties of conformally fabricated parts were significantly improved and could be adjusted by different toolpath designs.

The rest of this paper is structured as follows. Section 2 provides an overview of the workflow of the robotic conformal AM system of CFRP and details the proposed conformal toolpath generation method, which is the

major technology contribution of our study. Section 3 shows the application of the built AM system in a grid-stiffened conical shell structure of CFRP. Finally, conclusions are drawn in the last section.

2. Materials and methods

The robot-assisted conformal CFRP-AM system developed has a modular architecture, which facilitates system retrofitting and upgrading. The system is divided into four main modules: the host computer, robot-based multi-DoF motion module, fibre-polymer co-extrusion module, and the pre-fabricated substrate, as shown in Figure 2. The host computer is used for process planning and motion control. The multi-DoF device is based on a 6-axis robot. Although only five degrees of freedom are needed to position and orient the co-extrusion nozzle to points of an arbitrary surface. The additional DoF of the robot improves the smoothness of the toolpath by avoiding collisions and singularities. This robot arm (UR10e collaborative robot, Universal Robots LLC) is mounted on a vibration isolation platform, and it has a spherical working volume with a radius of 1300 mm and a payload capacity of 10 kg. Additionally, the robot has a position repeatability of 0.05 mm and a maximum TCP (Tool Center Point) velocity of 1000 mm/s. The co-extrusion module is attached to the robot end and includes a fibre extruder, polymer extruder, fibre cutting device, co-extrusion nozzle, and temperature control device. This in-house developed module has been optimised for processing CFRP. The nozzle exit has a diameter of 1 mm and is rounded to avoid fibre scraping. Also, the maximum heating temperature of the nozzle is 300 °C, above the melting point of most engineering thermoplastics. The freeform substrate is used for extruded composite adhesion to achieve high printing quality, and it should not be mounted too close to the edge of the robot workspace, as this increases the chances of reaching the joint limits. Moreover, the substrate can be made with various processes and reused.

The system works with three main steps: system calibration, conformal toolpath generation, and process implementation. As shown in Figure 3, the system starts with the system calibration in which the co-extrusion module and substrate are precisely calibrated to ensure high print quality. This step only needs to be run if any module is being replaced. Then to initiate a job, the workflow begins with a conformal toolpath generation method. Within the method, a proposed surface mapping-based path planning method was applied to generate the conformal paths of the shell and ribs first. The substrate has been precisely calibrated with

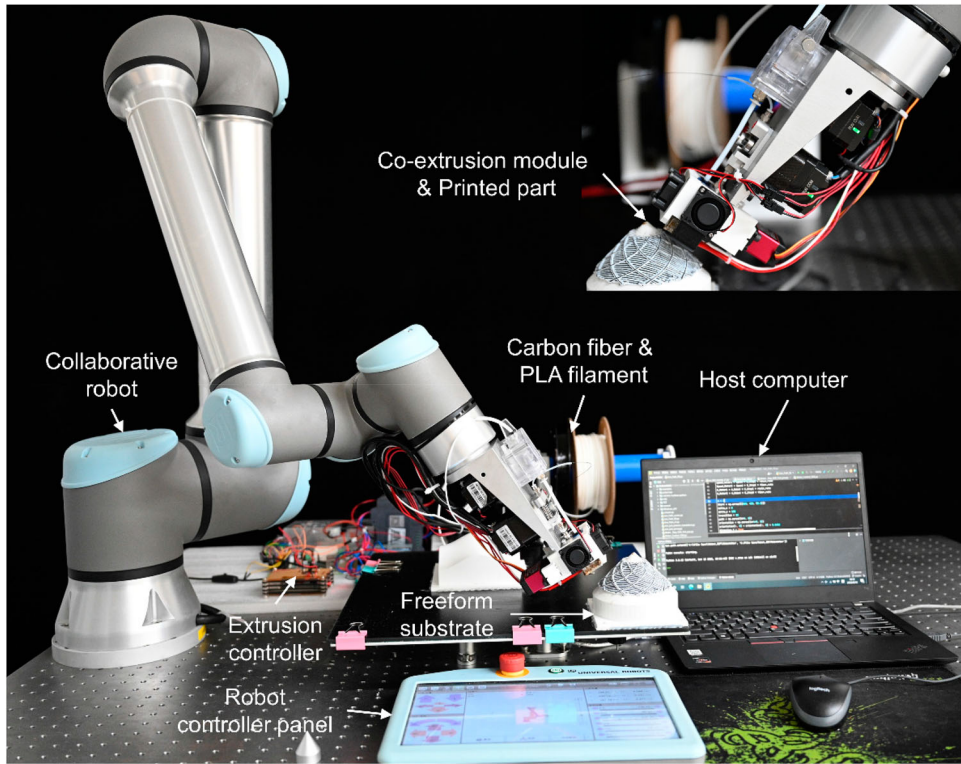


Figure 2. The setup of the robot-assisted CFRP-AM system.

respect to the robot during the system calibration step. Therefore, the generated paths can be described with respect to the robot base frame and thus converted into machine code, which includes robot trajectories

and composite co-extrusion rates. Within the method, key design parameters are adjustable, allowing their impact on print quality. These parameters include hatching patterns, layer thickness, single bead width,

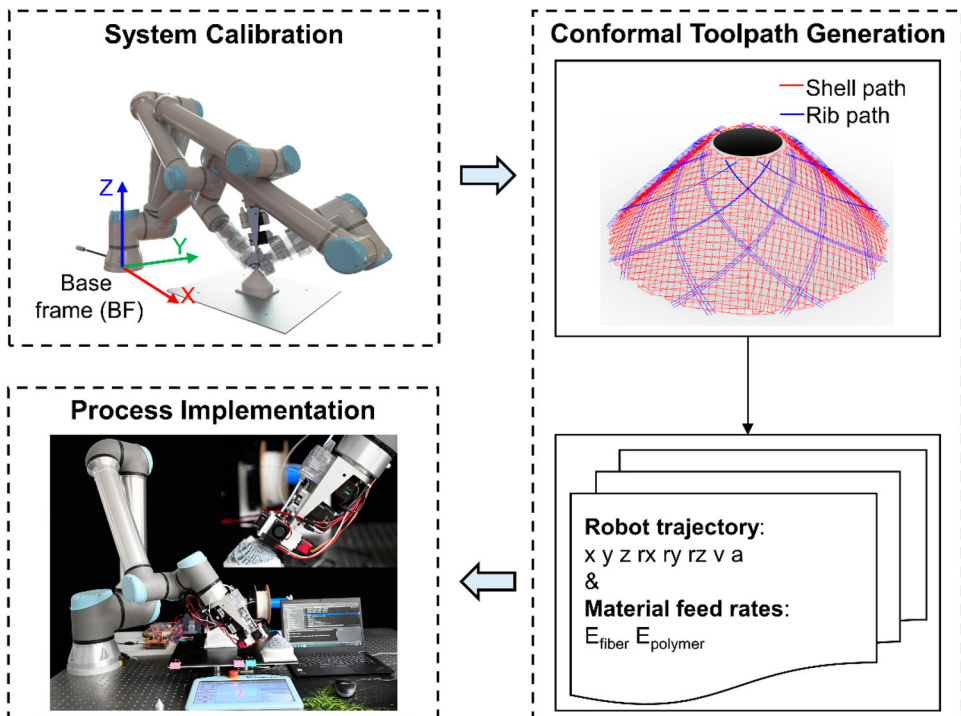


Figure 3. The robot-assisted conformal CFRP-AM system architecture.

and printing speed. Finally, the generated machine code was distributed to the robot and co-extrusion controllers for parts fabrication. More technical details are described below.

2.1 System calibration

During the printing process, a significant factor affecting the printing quality is the gap between the nozzle tip and the previous layer. Thus, the poses of the substrate and nozzle tip with respect to the robot must be calibrated to ensure the gap is precise and uniform across the entire work surface. In other words, the calibration process is to establish the mathematical description of the pose relationship between the substrate frame (SF) and tool centre frame (TCF) with respect to the base frame (BF). In addition to these three frames, an end frame (EF) built into the robot system is introduced to assist the calibration process, and the system frame setup is shown in Figure 4. The steps of the calibration process are as follows.

Step One: TCF calibration. The TCF is fixed at the co-extrusion nozzle tip, and its poses relative to the BF describe the position and posture of the nozzle with respect to the robot. Moreover, the data is represented using the transformation matrix $T = \begin{bmatrix} R & P \\ 000 & 1 \end{bmatrix}$, where R and P are the rotation matrix and translation vector, respectively. So, the transformation matrix B_T of TCF with respect to BF can be obtained as follow:

$${}^B_T = {}^B_E T * {}^E_T = \begin{bmatrix} {}^B_E R * {}^E_R & {}^B_E R * {}^E P_T + {}^B P_E \\ 0 0 0 & 1 \end{bmatrix}, \quad (1)$$

where B_T consists of the rotation matrix B_R and position vector B_P , which denotes the pose of EF with respect to

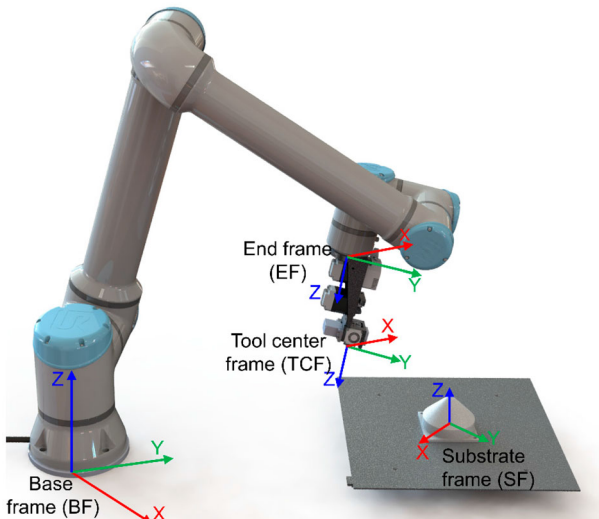


Figure 4. The system frames setup.

BF, and E_T consists of E_R and E_P , which denotes the pose of TCF with respect to EF. Matrix B_T could be calculated by the robot kinematic model which has been built into the robot controller. To calculate the transformation matrix E_T , a cone tip was fixed at an appropriate location in the robot workspace first. The robot was moved to make the nozzle tip centre coincide with the fixed cone tip at least 4 times in different postures. As shown in Figure 5(a), which illustrates the acquisition of two data points and the actual calibration process. The position vector remains the same due to the fixed cone tip remaining the same, as shown below:

$${}^B P_{Ti} = {}^B R_i * {}^E P_T + {}^B P_E, \quad (2)$$

where i denotes the i^{th} data point. The position vector ${}^E P_T = (x, y, z)$ of the TCF with respect to the EF also remains the same as the nozzle is fixed at the robot end. Therefore, the linear equation system $A * {}^E P_T = B$ can be obtained by subtracting any two data points, i.e. Eq (2), and then associating them. By using the linear least square method, the best fit of the position vector of TCF with respect to EF can be acquired, as:

$${}^E P_T = (A^T A)^{-1} A^T B, \quad (2)$$

As for the posture data of TCF with respect to the EF, the rotation matrix E_R is usually obtained directly from the mechanical design model.

Step Two: SF calibration. For getting the transformation matrix S_T of SF with respect to BF, the calibrated TCF is used in this step. As shown in Figure 5(b), there are usually three feature points defined on the substrate for calibration, usually the origin point P_0 of SF, the offset point P_1 on the x-axis, and a point P_2 on the XY plane. The position vectors of these points with respect to the BF are measured by moving the nozzle tip in contact with them. With the known correspondence between the features points, the transformation matrix can be easily constructed as follows: ${}^S_T = \begin{bmatrix} X & Y & Z & P_0 \\ 0 & 0 & 0 & 1 \end{bmatrix}$, where the X , Y , and Z are the vectors of X-axis, Y-axis, and Z-axis described in BF respectively, P_0 is the calculated origin coordinates of SF described in BF. Moreover, each feature point position should be measured multiple times to minimise errors.

2.2 Surface conformal toolpath generation method

In this study, a surface mapping-based algorithm was developed to design and generate conformal paths for the grid-stiffened shell structures of CFRP. These conformal paths were then translated into machine code for

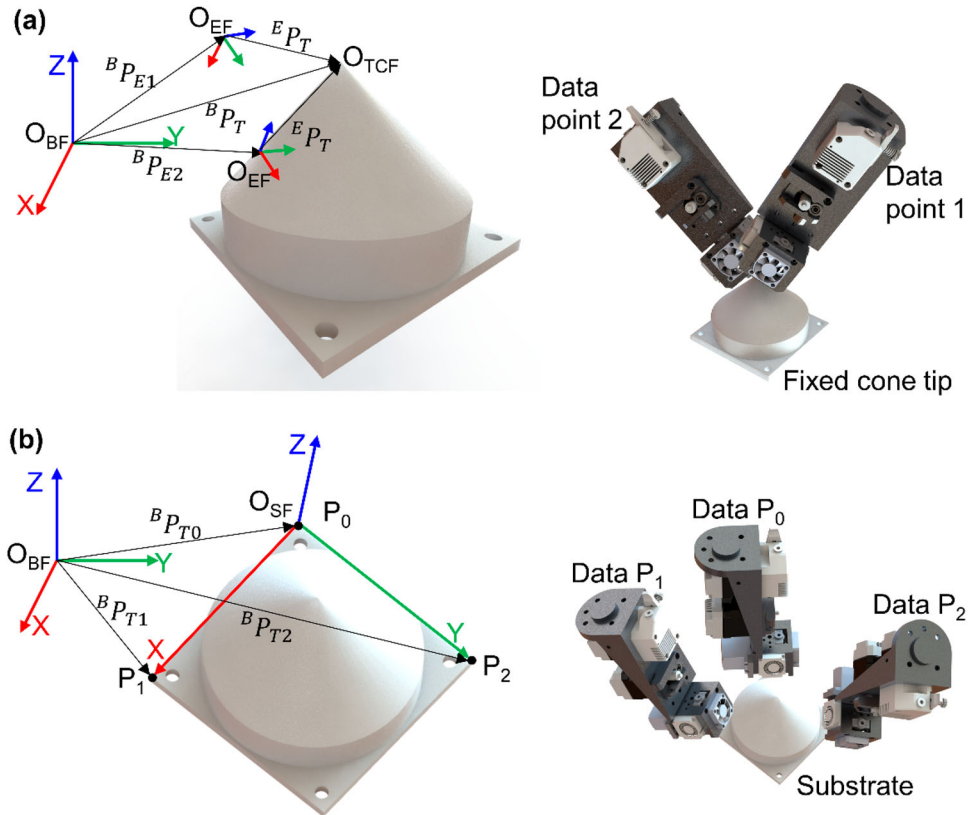


Figure 5. System frames calibration: (a) TCF calibration and (b) SF calibration.

machine motion control, including robot trajectories and material feed rates.

2.2.1 Surface mapping-based conformal path planning

The main challenge of conformal path planning is the Z value varies dynamically with the X-Y value within the same layer according to the shape of the free-form surface. To solve this challenge, the surfaces are mapped to 2D planes to simplify calculations. The workflow of this method is shown in Figure 6. Different from conventional slicing software, this method starts with the input of user-defined key structural parameters, such as the surface model of the calibrated substrate and structural thickness. In addition, the conformal CFRP-AM process is also layer-by-layer, a series of working surfaces need to be constructed by offsetting the developable surface for path planning first. These working surfaces will then be mapped to the 2D plane, and the shell-layer surfaces are mapped differently from the rib-layer surfaces. In the next step, various hatching patterns will be generated on these 2D planes, such as zigzag, contour, and cellular. These generated infill patterns will then be converted to 3D paths through the inverse mapping relationship. Finally, the generated 3D paths in all layers are combined and

stored as a series of ordered discrete points. Moreover, the surface normal vector corresponding to each point should also be calculated for subsequent robot trajectory. More details about the path planning method are provided below.

Step One: input the user-defined structural parameters. The input parameters include the designed shell surface, the normal thickness of shells (H_s) and ribs (H_r), and the layer thickness (h). The input surface is a developable surface that can be unfolded on a plane without any lap fold or break (Nelson et al. 2019; Bo et al. 2019). This feature ensures the feasibility of the surface unfolding in subsequent steps. Moreover, the developable surface discussed can be expressed by Eq. (4):

$$\mathbf{r}(u, v) = \mathbf{a}(u) + v\mathbf{b}(u), \quad (4)$$

where the trajectory curve $\mathbf{a}(u)$ is called directrix, and $\mathbf{b}(u)$ is the vector of the straight line which is called generatrix, u and v are the orthogonal curvilinear coordinate system in the parametric space. During the conformal CFRP-AM process, the slicing layers are obtained by offsetting the input surface model. Therefore, the normal thickness of shells and ribs and layer thickness were input to determine the offset distance of each sliced layer.

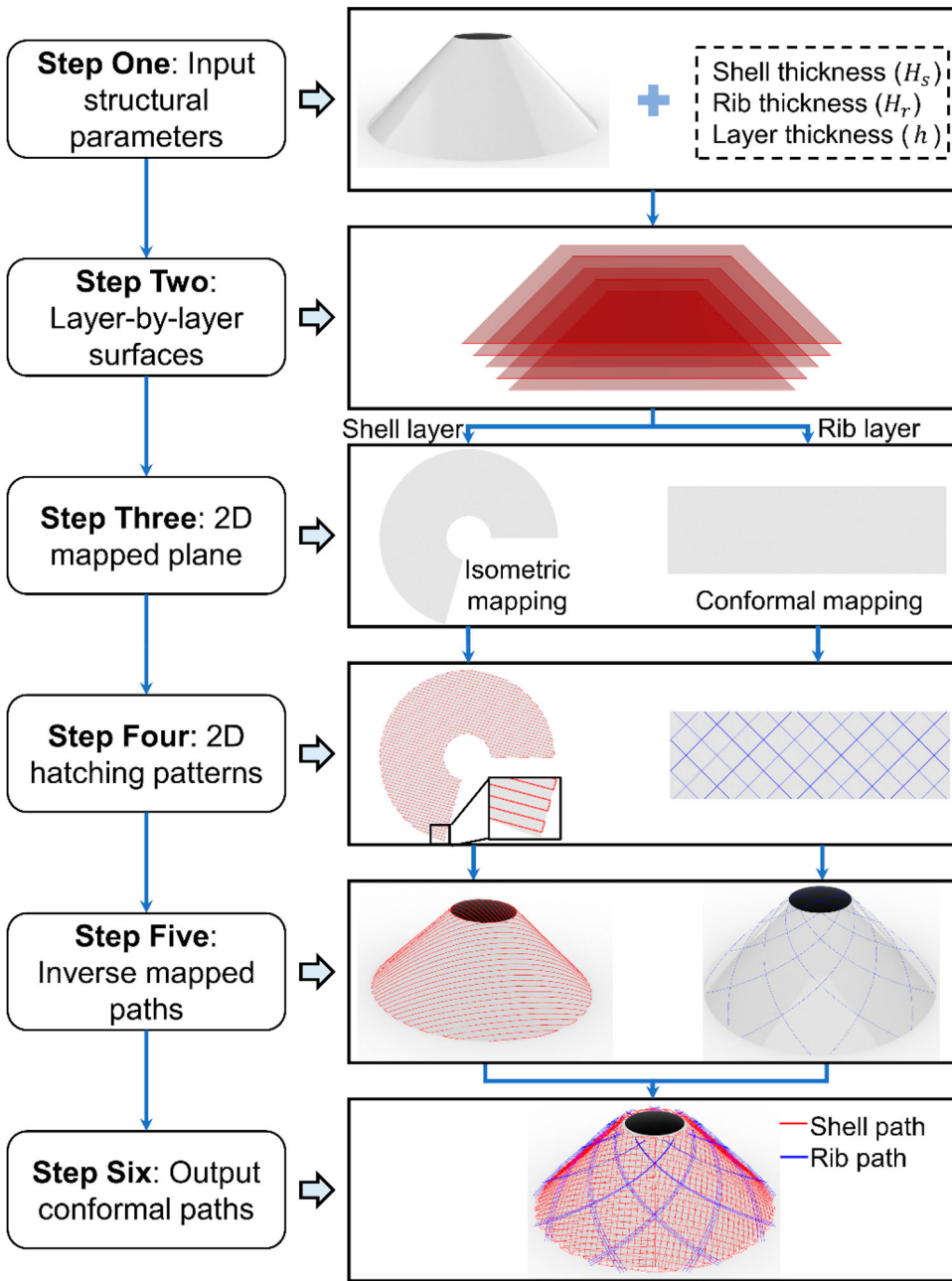


Figure 6. The workflow of the surface mapping-based conformal path planning method.

Step Two: construct the working surfaces. In this study, each working surface was generated by normal offsetting the input surface with an amount H , where $H = \text{layer thickness} \times \text{layer number}$, as shown in Figure 7(a). This normal offset vector can also be projected horizontally or vertically and corrected by a factor to ensure that the normal thickness remains constant. This normal offset was applied to maintain a constant layer thickness for better printing quality. In addition, each working surface is divided into a shell surface or a rib surface, depending on the location of the working surface.

Step Three: mapping each working surface to the 2D plane. Within the step, different mapping functions are used to meet different infill requirements of the shell surface and rib surface. Specifically, isometric mapping is used for the shell surface, while conformal mapping is used for the rib surface. First considering the shell surface, two surfaces associated with an isometric mapping can be fit to each other by continuous deformation despite their different shapes, and any corresponding curves on them have the same length. Thus, without changing the single bead width, the fully filled hatching patterns

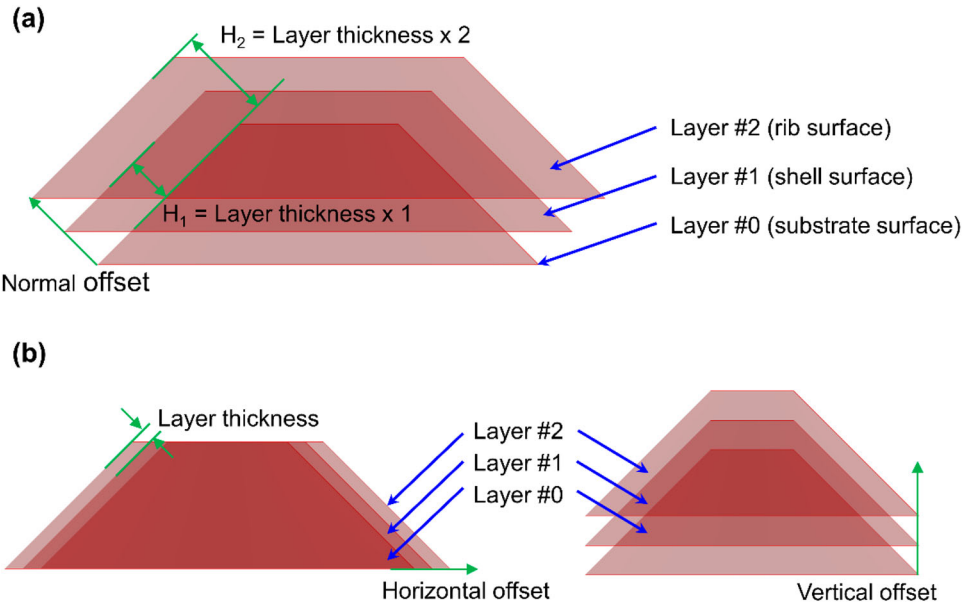


Figure 7. Generating the layer-by-layer surfaces by offsetting the surface: (a) along the normal vector, (b) along the horizontal vector or the vertical vector.

on the plane can also be served on the 3D surface. Moreover, all working surfaces are developable, which ensures that isometric mapping is available for these surfaces. The stiffened ribs distributed on the shell have a grid-based layout which is usually characterised by regular shapes defined as rectangular. These rectangles are often difficult to fill with the shape into the complex polygons generated by the isometric mapping. Thus, conformal mapping was used to map the rib surface to the 2D Euclidean plane, and it is a relaxation of the isometric mapping (Choi and Lui 2015). The theoretical basis for the conformal mapping is that, according to the uniformization theorem (Jin et al. 2022), the universal covering space of any surface with its uniformization conformal metric in \mathbb{R}^3 can be isometrically embedded onto one of the three canonical surfaces: sphere, plane, or hyperbolic space. Moreover, conformal mapping is angle-preserving, i.e. it maintains the local shape over the geometry. This helps to maintain the structural physical properties, such as the ribs angle which has a significant impact on the mechanical properties (Ehsani and Dalir 2019; Maes, Pavlov, and Simonian 2019).

The specific mapping theory is based on computational conformal geometry (Gu, Luo, and Yau 2010; Zhou, Gao, and Li 2022). Suppose S_1 and S_2 are two Riemann surfaces which are represented as $r_1(x^1, x^2)$ and $r_2(x^1, x^2)$, and $r_1, r_2: \mathbb{R}^2 \rightarrow \mathbb{R}^3$ are the vector-valued functions. In this study, S_1 is the working surface, and S_2 is the mapped 2D plane. The first fundamental

forms of S_1 and S_2 are respectively defined by:

$$d_{S_1}^2 = \sum_{ij} g_{ij} d_{x^i} d_{x^j}, \quad i, j = 1, 2, \quad (5)$$

$$d_{S_2}^2 = \sum_{m,n} \bar{g}_{mn} d_{x^m} d_{x^n}, \quad m, n = 1, 2, \quad (6)$$

where $g_{ij} = \frac{\partial r_1}{\partial x^i} \cdot \frac{\partial r_1}{\partial x^j}$ and $\bar{g}_{mn} = \frac{\partial r_2}{\partial x^m} \cdot \frac{\partial r_2}{\partial x^n}$, specifically for the developable surface discussed in this study, x^1 and x^2 respectively denote the parameters u and v , as shown in Eq (2). The mapping function $f: S_1 \rightarrow S_2$ between two surfaces can be represented as $f: \mathbb{R}^2 \rightarrow \mathbb{R}^2$, $f = (f^1(x^1, x^2), f^2(x^1, x^2))$. The pull-back metric $f^* d_{S_2}^2$ is induced by f and $d_{S_2}^2$, which is further expressed as an analytic formula (Gu et al. 2004):

$$f^* d_{S_2}^2 = \sum_{mn} \left(\sum_{ij} \bar{g}_{ij}(f(x^1, x^2)) \frac{\partial f^m}{\partial x^i} \frac{\partial f^n}{\partial x^j} \right) d_{x^m} d_{x^n}. \quad (7)$$

It is always possible to find a coefficient function $\lambda(x^1, x^2)$ such that Eq. (8) holds:

$$f^* d_{S_2}^2 = \lambda(x^1, x^2) d_{S_1}^2, \quad (8)$$

and the function λ is called the conformal factor. When the conformal factor $\lambda = 1$, the mapping function f is an isometric mapping, and if the conformal factor is always positive, then f is a conformal mapping (Khamayseh and Wayne Mastin 1996; Konaković et al. 2016). The parametrization process of the developable surface is shown in Figure 8. Moreover, the derivation of the

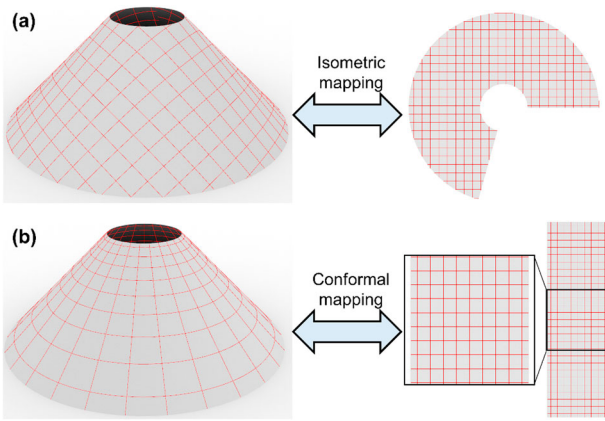


Figure 8. Surface mapping process, (a) isometric mapping, (b) conformal mapping.

mapping function with the conical surfaces as an example is shown in Appendix A.

Step Four: generate various hatching patterns within the 2D plane. In this step, various planar-layer-based infill algorithms are used to generate the hatching patterns in the mapped 2D plane. As shown in Figures 9 and 10, zigzag, arc offset-based, and contour offset-based hatching patterns are generated for fully filling the shell surface. Moreover, the filling parameters such as the single bead width and fibre filling angle for the zigzag pattern can be adjusted within a certain range.

The 2D sparse hatching patterns are filled within the conformally mapped rectangle to generate the stiffened ribs configuration distributed on the shell, while the pattern is also the toolpath. The hatching patterns are formed by straight lines with different angles

that are evenly spaced along the parametric axes (u and v) and cross each other, as shown in Figure 10(a–c). During this process, the angle and number of straight lines can be adjusted to produce various cellular structures. In addition, more complex cellular patterns can be generated by filling various basic cells, as shown in Figure 10(d).

Step Five: mapping back the 2D hatching patterns to the 3D surface. The mapping function f is homogeneous, i.e. the mapping function is one-to-one (Gu et al. 2012). Hence, for any surface in this study, this mapping relationship can also be written by:

$$r(u, v) = r(f^{-1}(u, v)), \quad (9)$$

where f^{-1} represents an inverse mapping operator. Thus, the orthogonal curvilinear coordinate system of the shell or rib surface can be obtained by the mapping parameterisation:

$$(x, y, z) = (r_1(f^{-1}(u, v)), r_2(f^{-1}(u, v)), r_3(f^{-1}(u, v))). \quad (10)$$

The results of mapping back to the 3D surface via the inverse mapping function f^{-1} was shown in Figures 9 and 10.

Step Six: store the generated conformal paths with an ordered set of discrete points and their normal vectors. The generated conformal paths would be sorted layer by layer first. Then the conformal paths are divided into segments within the allowed error range and the endpoints of the segments are stored. It is also necessary to calculate and store the normal vector corresponding to each point for the next step of robot trajectory calculation.

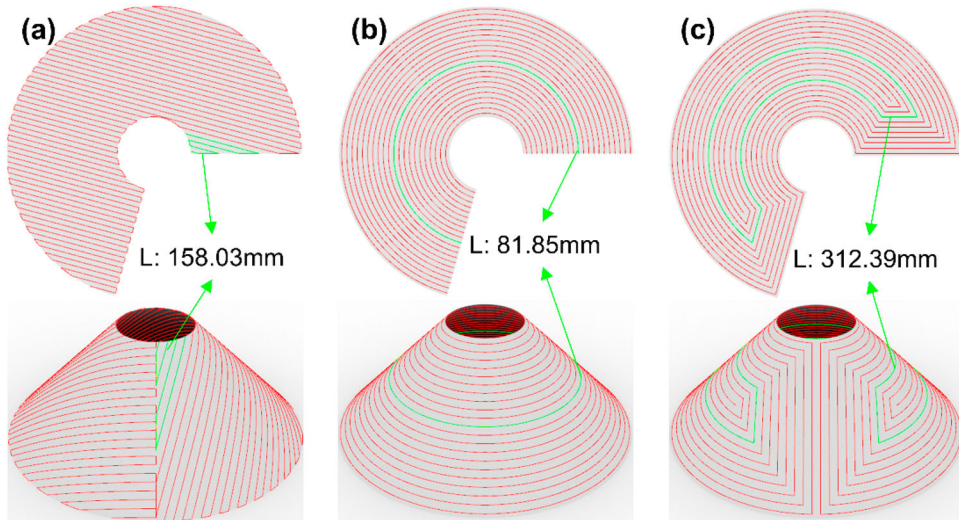


Figure 9. Various toolpaths generated by isometric mapping for fabricating the shell: (a) zigzag, (b) arc offset-based, and (c) contour offset-based.

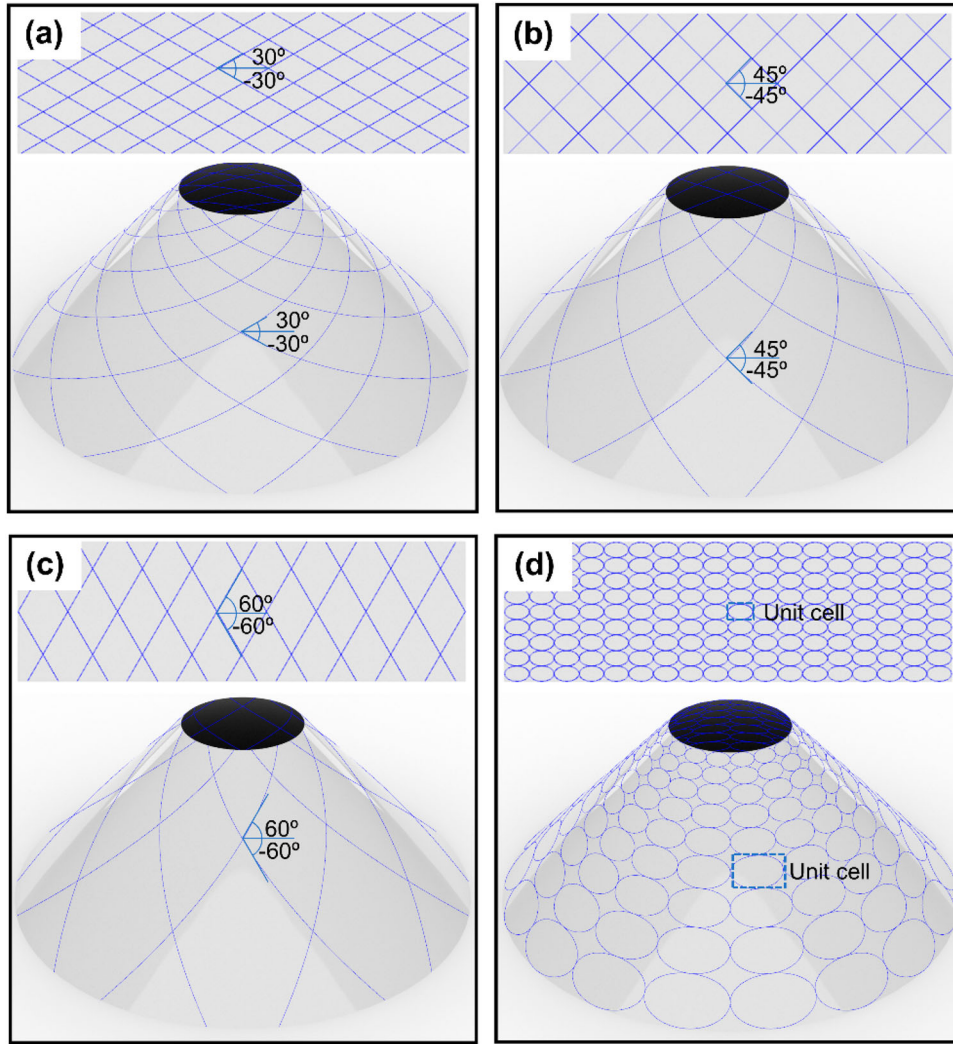


Figure 10. Various configurations generated by conformal mapping for fabricating the stiffened ribs, (a) cross lines with $\pm 30^\circ$, (b) cross lines with $\pm 45^\circ$, (c) cross lines with $\pm 60^\circ$, and (d) rectangular units with ellipse fill.

2.2.2 Machine code generation

Step One: robot trajectory generation. To guide the robot's motion, the generated conformal paths need to be converted into a series of ordered TCF poses including tool positions and orientations, as shown in

Figure 11(a). The generated conformal paths above were stored with discrete points and the corresponding normal vectors (\mathbf{n}) with respect to the SF. During the printing process, the Z_i -axis of TCF is forced to align with the normal vector at each discrete waypoint of

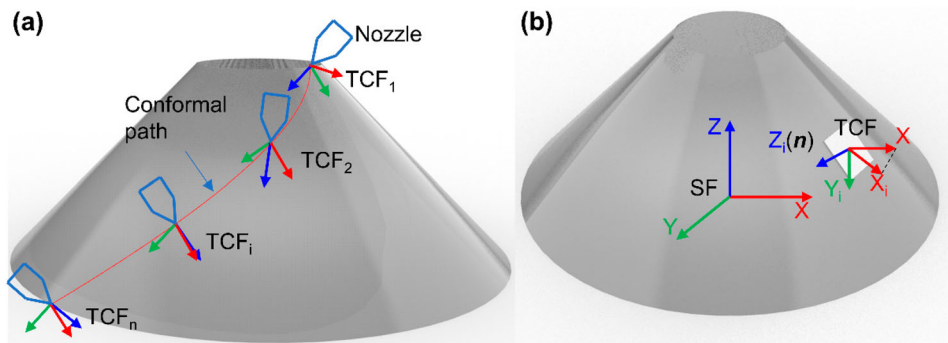


Figure 11. Robot trajectory generation, (a) the nozzle poses (TCF) generation for waypoints along the conformal path, (b) the TCF construction at a discrete waypoint.

the conformal path. Therefore, a series of TCF poses is constructed with the discrete points as origins and the unitised normal vector as the Z_i -axis. As for the X_i and Y_i axes of the TCF, any two orthogonal vectors in the Z_i -axis normal plane can be selected. This is because the nozzle tip is circular and its rotation around the Z_i -axis has little effect on the deposition of the single bead. In this study, the projection vector of the SF X_i -axis vector on the normal plane of the TCF Z_i -axis vector was unitised to create the TCF X_i -axis vector, as shown in Figure 11(b). The Y_i -axis vector was calculated by the cross-product of the Z_i and X_i axes' vectors. The TCF with respect to the SF was constructed with the three calculated axis vectors and the discrete point coordinates, which could be abbreviated as

$${}^S T_i = \begin{bmatrix} X_i & Y_i & Z_i & P_i \\ 0 & 0 & 0 & 1 \end{bmatrix}, \text{ where the } i \text{ denotes the } i^{\text{th}} \text{ point}$$

data. Then the constructed TCF poses are translated to the BF, and the transformation matrix was as follows: ${}^B T_i = {}^S T * {}^S T_i$. Finally, the transformation matrix is usually converted to a more concise vector form $[x, y, z, r_x, r_y, r_z]$, where $[x, y, z]$ is the origin coordinate and $[r_x, r_y, r_z]$ is rotation vector used for the UR robot. Moreover, the motion control based on joints vector $\theta = [\theta_1, \theta_2, \dots, \theta_6]$ can be calculated by inverse kinematics for a given TCF pose. The inverse kinematic problem can be solved using the analytical or numerical iterative methods with the robot kinematic chain model, i.e. D-H parameters.

Step Two: composite materials feed rates generation. To produce high-quality parts, this system requires the material extrusion rates to be precisely synchronised with the robot's conformal motion. More specifically, the interaction between robot kinematics and deposition process parameters along the conformal printing paths needs to be modeled and well-controlled. Hence, the section of a rectangular sample was observed with the scanning electron microscope (SEM), as shown in Figure 12(a). The deposited single bead could be represented as rounded rectangles with semi-wrapped fibre bundles. In this study, the single layer thickness (h) and the single bead width (w) were used to describe the cross-sectional shape, as shown in Figure 12(b). Meanwhile, E_1 and E_2 denote the feed rates of fibre and polymer filament fed into the printing head. For a given printing speed (v), E_1 has a significant effect on fibre alignment and thus on the mechanical properties of the printed part. Thus, a correction factor k_1 is introduced to adjust the fibre alignment, and it is usually set to 0.95-1.0. Similarly, the E_2 is also adjusted by a correction factor k_2 . As shown in Figure 12(b), there are gap areas in the printed part in the standard model of the multi-bead deposition model. Thus, k_2 is usually set to

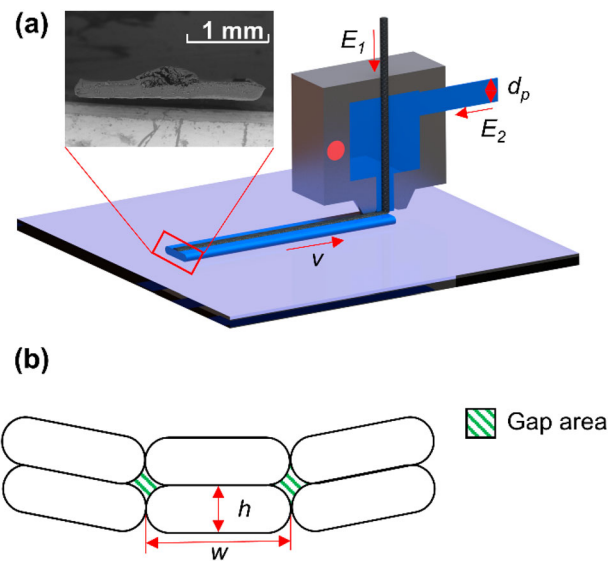


Figure 12. (a) Deposition process modeling and SEM of the deposited single bead, (b) multi-bead cross-section model.

1.0-1.15 to reduce the voids in this study. The fewer voids often contribute to improved mechanical properties. According to the volume conservation principle, the relationship between the feed rates of materials and printing speed is quantified as below:

$$\begin{cases} E_1 = k_1 v \\ E_2 = 4k_2 v h w / (\pi d_p^2) \end{cases} \quad (11)$$

where the printing speed v , the single-layer thickness h , the single bead width w , the polymer filament diameter d_p , and the correction factors k_1 and k_2 are user-determined. Besides, the feed rates of materials need to be translated into the control pulse frequencies to guide the corresponding motor rotation.

2.3 Process implementation

In this step, the machine code is decoded and distributed to the corresponding module controller. Specifically, the temperature data is first sent via serial communication to the co-extrusion controller. A built-in PID control programme controls the heating of the nozzle with a specified temperature. Then the control commands for the robot's motion are sent through the Ethernet to the robot controller. Simultaneously, the calculated composite feed rates are streamed to the co-extruder controller. After each sub-path is printed, the material feed is stopped, and a cutting command is sent to drive the servo for fibre cutting. Once all paths are printed, the host computer sends a command to terminate nozzle heating and the robot is moved to a safe position, then the user removes the printed part.

2.4 Case study

2.4.1 Grid-stiffened shell structure construction

The case study considers a typical grid-stiffened shell structure, and its geometric parameters are shown in Figure 13. The shell structure is based on a flat-topped conical surface, which is a typically developed surface. The diameter of the bottom circle of the basic conical surface is 80 mm, the diameter of the top circle is 20 mm, and the height is 30 mm. The stiffened ribs are designed based on cross lines at the $\pm\theta$, as shown in Figure 10(a). The normal thickness of the shell and ribs are set to 1.2 and 1.5 mm, respectively. For fairness of comparison, as many printing parameters as possible are consistent in both processes.

2.4.2 Materials and experiment setup

To illustrate the advantage of the conformal CFRP-AM process, the designed grid-stiffened shell structure was fabricated using both the proposed robotic and conventional 3-axis CFRP-AM systems. The 3-axis platform used was the Anisoprint Composer A4 printer (Anisoprint LLC), which runs with the commercial slicing software Aura (Anisoprint Aura 1.27, © 2020 Anisoprint LLC). The fibre reinforcement utilised in this study is reinforced with a carbon fibre (Anisoprint LLC) which is pre-impregnated with thermosets, and it is 1.5k with an effective diameter of 0.35 mm. The polymer matrix is the PLA filaments (Polymaker LLC) that have an effective diameter of 1.75 mm and have been dried at 60 °C for 10 h before printing.

For fairness of comparison, as many printing parameters as possible are consistent in both processes. The default print parameters for all cases are set as follows: nozzle temperature of 200 °C, and print speed of 9 mm/s for the fibre-polymer co-extrusion nozzle. The difference is that, due to the structure size, Anisoprint can only fill the shell area with fibres, while the rib area requires an additional pure polymer extrusion head with a speed of 50 mm/s to print. In addition, the default deposition parameters of Anisoprint are as

follows: 0.65 mm single bead width and 0.34 mm layer thickness for the fibre-polymer co-extrusion head, and 0.4 mm single bead width and 0.17 mm layer thickness for pure polymer extrusion head. The robot-assisted system sets the single bead width at 2 mm and the normal layer thickness at 0.3 mm. Moreover, the bed temperature in the planar process is set to a default value of 40 °C. Meanwhile, the conformal process fabricates parts on a freeform substrate made of Nylon. The temperature of the substrate is maintained at room temperature, which is approximately 25 °C.

The performance of the parts fabricated with different processes and toolpaths was illustrated by the compressive strength and stiffness of the fabricated components. For each design, three samples were fabricated and characterised to illustrate the reproducibility of the constructed system. The structure compression properties were characterised through the quasi-static compression tests on a 20 kN universal material testing machine (Z2020, ZwickRoell, Germany) with a fixed loading rate of 4 mm/min.

3. Results and discussion

3.1 Experimental results

The specimens for the compression test and their force-displacement curves are shown in Figure 14. The test structure consists of a flat-topped conical shell and stiffened ribs designed based on cross lines at the $\pm 45^\circ$. The shell and rib features were fabricated with both planar and conformal processes for comparison. Part 1-1 was sliced and fabricated by a commercial 3-DoF CFRP-AM machine, where the shell can be filled with one fibre per layer with a total fibre length of 14.5 m, while the non-planar stiffened ribs cannot be filled with fibres. As for Part 1-2, the conical shell is fabricated with the planar process, the stiffened ribs are conformally fabricated by the robot-assisted system, and the total fibre length of the ribs is 3.24 m. Compared to Part 1-1, the conformally fabricated ribs increased the

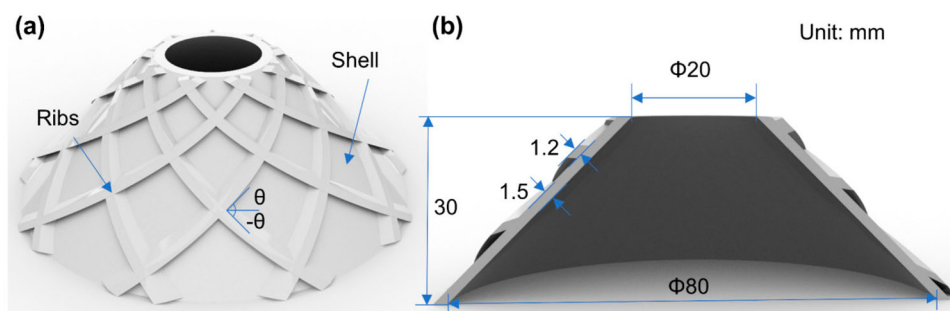


Figure 13. Geometric parameters of the grid-stiffened conical shell structure: (a) oblique view and (b) cross-sectional view.

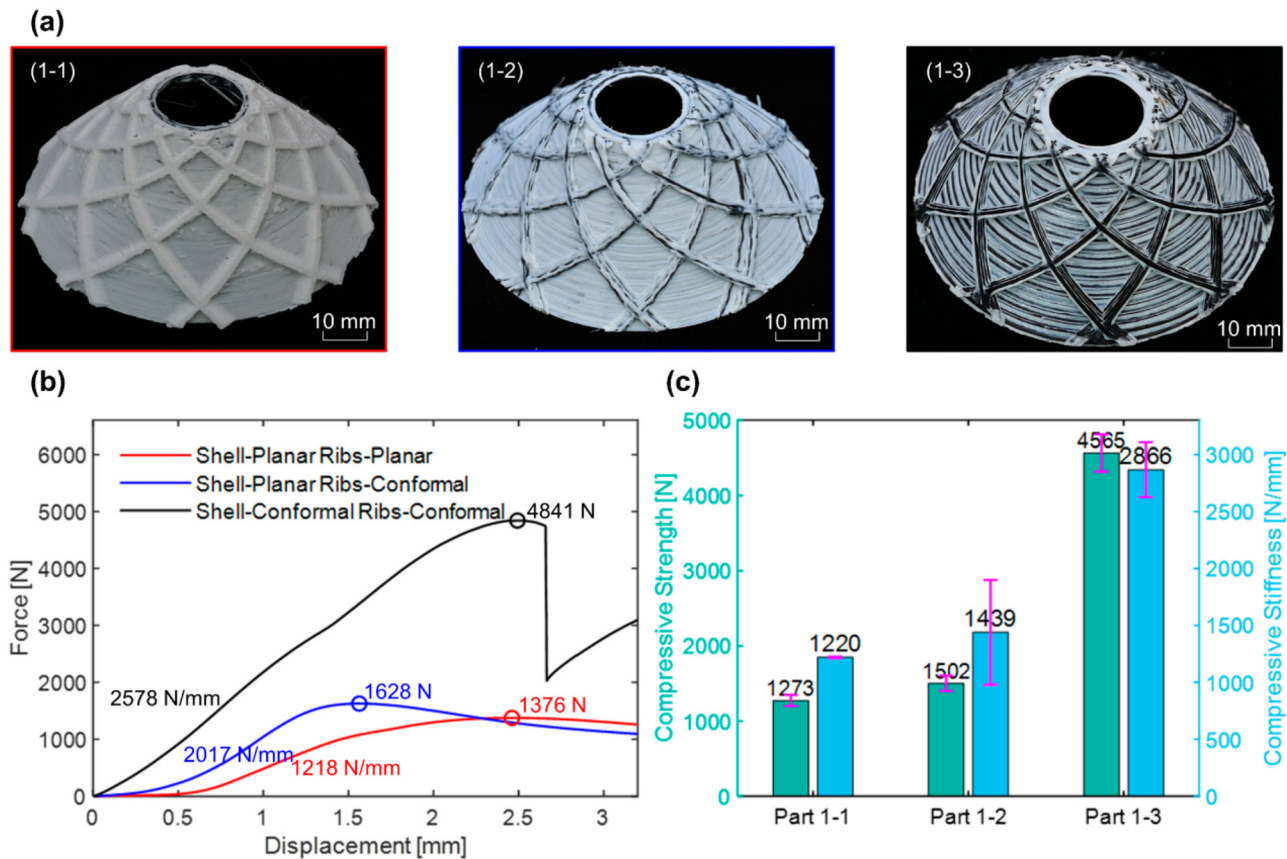


Figure 14. The fabricated samples with different processes and their compression performance: (a) the fabricated samples, (b) the force-displacement curves, and (c) compressive strength and compressive stiffness.

compressive strength of the structure by 18.0% and the compressive stiffness by 17.9%. Part 1-3 with shell and ribs fabricated by the conformal process has the highest compression strength and stiffness, which are 258.6% and 134.9% higher than Part 1-1, respectively. In addition, the total fibre length of Part 1-3 is only 14.2 m.

The conformal CFRP-AM process allows for greater flexibility in fibre orientation design. Due to the significant anisotropy of CFRP, the parts with different toolpaths also have different mechanical properties. Hence, the parts with different toolpaths were fabricated and tested to illustrate the effect of fibre orientation on structural properties. The effect of different toolpaths in the conical shell was first verified by two cases, i.e. the arc offset-based (2-1) and zigzag (2-2), as shown in Figure 9 and Figure 15. The stiffened ribs were based on the $\pm 45^\circ$ hatching grid pattern, as shown in Figure 10(b). Part 2-1 with an arc offset-based hatching pattern has higher compression strength and stiffness for 4565 and 2866 N/mm, respectively.

The effect of different rib configurations was then also tested in three cases, as shown in Figure 16. The stiffened ribs structures were designed based on cross

lines at different angles, respectively $\pm 30^\circ$, $\pm 45^\circ$, and $\pm 60^\circ$, as shown in Figure 10. The conical shell was fabricated with the arc offset-based paths, as shown in Figure 9(b). The three components exhibit different properties in terms of compressive strength and stiffness, with Part 3-2 ($\pm 45^\circ$) having the highest compressive strength of 4565 N and Part 3-3 ($\pm 60^\circ$) having the highest compressive stiffness of 3883 N/mm, respectively.

3.2 Discussion

The above results manifest that the conformal CFRP-AM process can effectively fabricate grid-stiffened shell structures with greatly improved mechanical properties. Comparing the two different processes, the key difference is that the conformal CFRP-AM process uses multi-DoF motion to directly fabricate curved surface layers. The conventional process confines the fibres within a planar layer and does not enhance the structure along the stacking direction. The curved slicing layers allow continuous fibre distribution along the curved surfaces to overcome this disadvantage. As shown in Figure 14, the conformally fabricated part 1-3 has a 93.3% increase in compression strength and a 71.3% increase

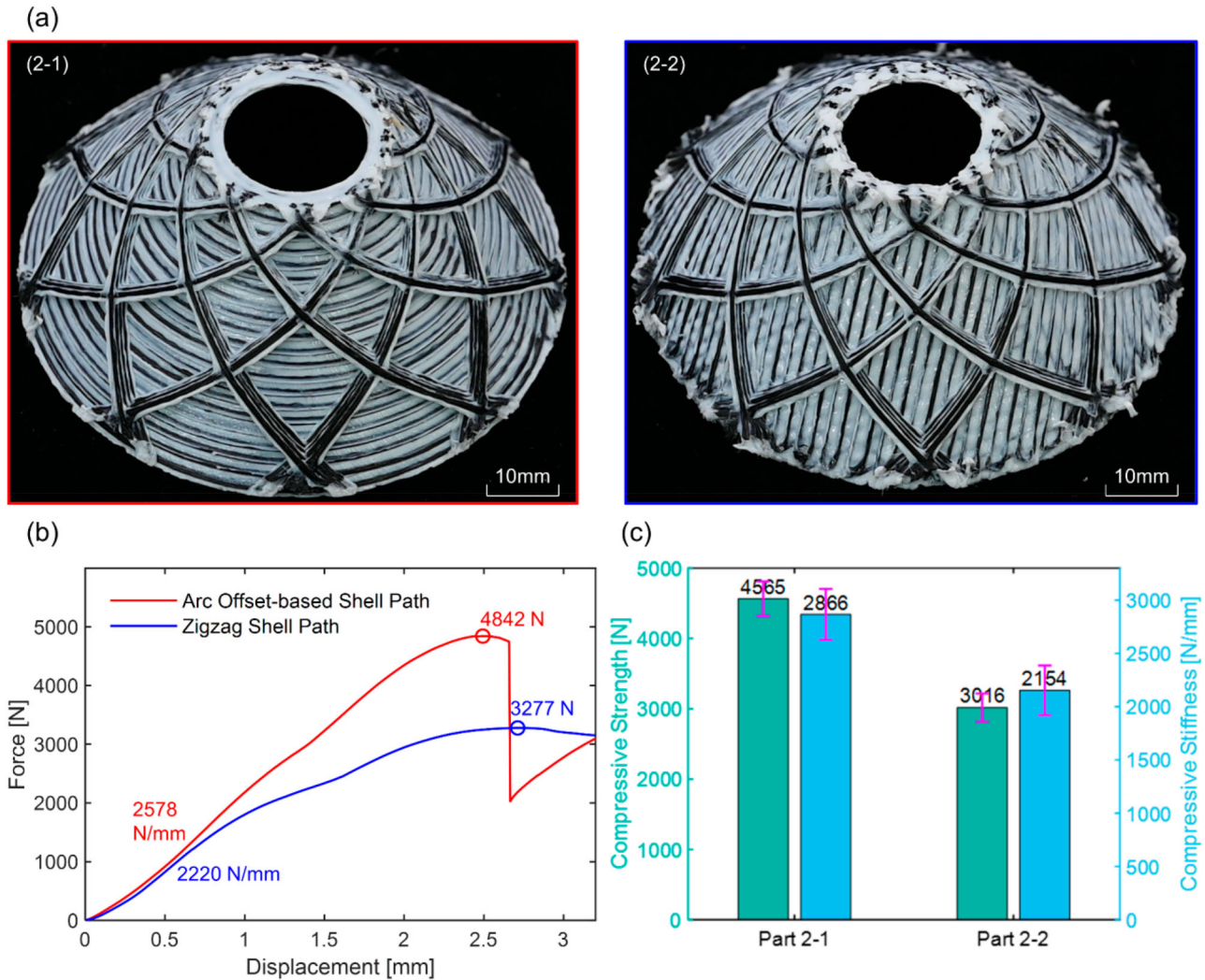


Figure 15. The fabricated samples with two shell toolpaths, i.e. (2-1) arc-offset pattern and (2-2) zigzag pattern, and their compression performance: (a) the fabricated samples, (b) the force-displacement curves, and (c) compressive strength and compressive stiffness.

in stiffness. However, as shown in Figure 14(c), the mechanical properties of the samples fabricated by the robot-assisted conformal CFRP-AM system fluctuate more. The fabrication process shows that these performance fluctuations may originate from the motion instability of the print head, which is caused by the low structural stiffness and highly nonlinear joint motion of the robot. Therefore, further efforts will be made to improve the stability of the system.

The above results also illustrate that the same structure fabricated using different toolpaths has a diverse mechanical behaviour, which is caused by the CFRP anisotropy. The conformal CFRP-AM process leads to a more varied fibre orientation, which implies a greater structural performance regulation range. For example, with the same stiffened ribs, the shell with the arc offset-based toolpath has 26.2% higher compression strength and 33.1% higher compression stiffness than the shell with the

zigzag toolpath. This is because the deformation of the conical shell transforms the compression stress into tensile stress along the circumferential direction. This transformation allows structures with the arc offset-based toolpath to better utilise the excellent axial mechanical properties of CFRP. Therefore, optimising the toolpath considering the structural load distribution has great potential to further improve the mechanical performance of the structure, and this will also be a subject of further exploration. In addition to regulating structural strength and stiffness, more diverse fibre orientation designs hold great potential for creating structures with multiple functionalities (Wang et al. 2022; Lingappan et al. 2022; Goh et al. 2021). For example, the energy-absorbing and vibration-isolating structures based on fibre paths, sensing devices using fibre conductivity and thermal conductivity, and shape morphing devices based on fibre-matrix strain mismatch.

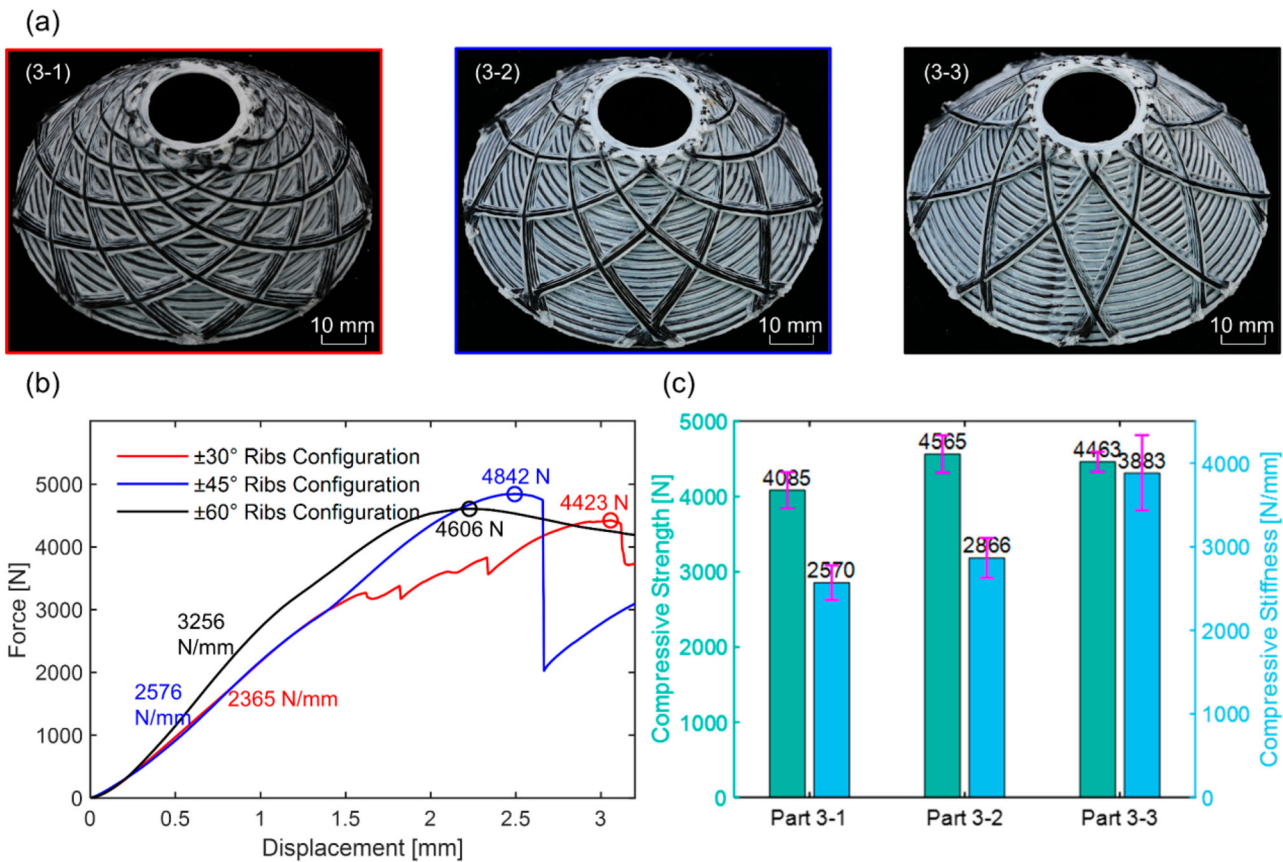


Figure 16. The fabricated shells reinforced by cross-line stiffener ribs with three configurations, i.e. $\pm 30^\circ$, $\pm 45^\circ$, and $\pm 60^\circ$, and their compression performance: (a) the fabricated samples, (b) the force-displacement curves, and (c) compressive strength and compressive stiffness.

Moreover, the conformal process can effectively improve material utilisation and manufacturing efficiency due to the support-free feature and less discontinuous toolpath. It also enhances the surface quality of the part by reducing the step-stair effect. In summary, the conformal process will effectively advance the transformation of AM into a reliable production option.

4. Conclusions

This study presents a robot-assisted conformal CFRP-AM system for grid-stiffened shell structures. The robotic multi-DoF motion allows the system to perform rapid exploration for selectively and spatially distributed reinforcement, thus promoting the CFRP-AM process as a viable production option. Each step of the system workflow was detailed, and the major step, i.e. conformal toolpath generation, was highlighted. The proposed conformal toolpath generation method allows the simultaneous generation of various fully filled toolpaths for developable shells and geometric designs for stiffened ribs. Also, this method is based on surface mapping with relatively low computational complexity.

Moreover, the compression experiments of components fabricated by different processes (planar and conformal-based) manifest that this conformal CFRP-AM system and its workflow can significantly improve the compression strength and stiffness of grid-stiffened shell structures. Also, the experimental comparisons made between parts fabricated with different toolpaths (shells filled with zigzag and arc-offset patterns) and various geometric designs (stiffener ribs with different crossline angles) demonstrate the additional design freedom of conformal CFRP-AM. This is another important advantage of the conformal CFRP-AM process, where the more diverse fibre orientation can be used to meet more diverse customisation needs, such as specific mechanical behaviour.

The following topics are suggested for further research on the conformal CFRP-AM process. Firstly, considering the needs of complex structures in actual production, the linkage of geometry-process-property and optimised motion control methods should be advanced. Secondly, the surface mapping-based conformal path planning method needs to be further developed. Within the method, due to the different scaling rates

of each point, the conformal mapping function can only ensure that the angle of the generated 3D hatching pattern remains the same, but the length changes. To overcome this limitation, a more advanced 2D filling method utilising resizable cells that uses resizable cells needs to be developed, allowing for the design of any desired 3D hatching pattern. Thirdly, more advanced conformal toolpath generation methods should be further explored to incorporate more design constraints for satisfying specific functional requirements such as energy absorption and thermal insulation.

Acknowledgment

This work is supported by the National Key Research and Development Program of China [Grant No.2021YFB1715400], the National Natural Science Foundation of China [Grant No.52105261], and the Shenzhen Science and Technology Innovation Commission [Grant No. JCYJ20210324104610028].

Disclosure statement

No potential conflict of interest was reported by the author(s).

Funding

This work was supported by National Natural Science Foundation of China: [grant number 52105261]; National Key Research and Development Program of China: [grant number 2021YFB1715400]; Shenzhen Science and Technology Innovation Commission: [grant number JCYJ20210324104610028].

Notes on contributors

Guoquan Zhang is a master's student at Southern University of Science and Technology, and his research interests include robot-assisted additive manufacturing for composites.

Yaohui Wang is a Ph.D. candidate at Southern University of Science and Technology. His research interests include continuous fibre reinforced plastic composite 3D printing and 4D printing.

Ziwen Chen is a research assistant at Southern University of Science and Technology, and he worked on the process improvement of Continuous fibre-reinforced polymer additive manufacturing.

Xuguang Xu is a master's student at Southern University of Science and Technology. His research interests include 3D printing, numerical simulation for 3D printing, and automated fibre placement.

Ke Dong is currently a collaborative Ph.D. student at the The Hong Kong Polytechnic University and Southern University of Science and Technology. His research interests include 3D/4D printing, fibre-reinforced composite and AI assisted-design.

Yi Xiong is an assistant professor at Southern University of Science and Technology, China. He received his Ph.D. degree in Engineering Design and Production from Aalto University,

Finland, in 2016. His research interests include additive manufacturing for composites and design for additive manufacturing.

ORCID

Yi Xiong  <http://orcid.org/0000-0002-0184-8607>

References

- Alhijaily, Abdullah, Zekai Murat Kilic, and A. N. Paulo Bartolo. 2023. "Teams of Robots in Additive Manufacturing: A Review." *Virtual and Physical Prototyping* 18 (1), doi:[10.1080/17452759.2022.2162929](https://doi.org/10.1080/17452759.2022.2162929).
- Alkadi, Faez, Kyung Chang Lee, Abdullateef H. Bashiri, and Jae Won Choi. 2020. "Conformal Additive Manufacturing Using a Direct-Print Process." *Additive Manufacturing* 32 (March): 100975. doi:[10.1016/j.addma.2019.100975](https://doi.org/10.1016/j.addma.2019.100975).
- Badarinath, Rakshith, and Vittaldas Prabhu. 2021. "Integration and Evaluation of Robotic Fused Filament Fabrication System." *Additive Manufacturing* 41 (May): 101951. doi:[10.1016/j.addma.2021.101951](https://doi.org/10.1016/j.addma.2021.101951).
- Bhatt, Prahar M., Ariyan M. Kabir, Max Peralta, Hugh A. Bruck, and Satyandra K. Gupta. 2019. "A Robotic Cell for Performing Sheet Lamination-Based Additive Manufacturing." *Additive Manufacturing* 27 (May): 278–289. doi:[10.1016/j.addma.2019.02.002](https://doi.org/10.1016/j.addma.2019.02.002).
- Bhatt, Prahar M., Rishi K. Malhan, Aniruddha v. Shembekar, Yeo Jung Yoon, and Satyandra K. Gupta. 2020. "Expanding Capabilities of Additive Manufacturing Through Use of Robotics Technologies: A Survey." *Additive Manufacturing* 31 (January): 100933. doi:[10.1016/j.addma.2019.100933](https://doi.org/10.1016/j.addma.2019.100933).
- Bi, Danjie, Fubao Xie, and Kai Tang. 2021. "Generation of Efficient Iso-Planar Printing Path for Multi-Axis FDM Printing." *Journal of Manufacturing and Materials Processing* 5 (2): 59. doi:[10.3390/jmmp5020059](https://doi.org/10.3390/jmmp5020059).
- Billah, Kazi Md Masum, Fernando A.R. Lorenzana, Nikki L. Martinez, Ryan B. Wicker, and David Espalin. 2020. "Thermomechanical Characterization of Short Carbon Fiber and Short Glass Fiber-Reinforced ABS Used in Large Format Additive Manufacturing." *Additive Manufacturing* 35 (October): 101299. doi:[10.1016/j.addma.2020.101299](https://doi.org/10.1016/j.addma.2020.101299).
- Bo, Pengbo, Yujian Zheng, Xiaohong Jia, and Caiming Zhang. 2019. "Multi-Strip Smooth Developable Surfaces from Sparse Design Curves." *Computer-Aided Design* 114 (September): 1–12. doi:[10.1016/J.CAD.2019.05.001](https://doi.org/10.1016/J.CAD.2019.05.001).
- Chen, Xiangjia, Guoxin Fang, Wei Hsin Liao, and Charlie C.L. Wang. 2022. "Field-Based Toolpath Generation for 3D Printing Continuous Fibre Reinforced Thermoplastic Composites." *Additive Manufacturing* 49 (January), doi:[10.1016/J.ADDMA.2021.102470](https://doi.org/10.1016/J.ADDMA.2021.102470).
- Choi, Pui Tung, and Lok Ming Lui. 2015. "Fast Disk Conformal Parameterization of Simply-Connected Open Surfaces." *Journal of Scientific Computing* 65 (3): 1065–1090. doi:[10.1007/s10915-015-9998-2](https://doi.org/10.1007/s10915-015-9998-2).
- Cui, Xiangyang, She Li, Hui Feng, and Guangyao Li. 2017. "A Triangular Prism Solid and Shell Interactive Mapping Element for Electromagnetic Sheet Metal Forming Process." *Journal of Computational Physics* 336 (May): 192–211. doi:[10.1016/J.JCP.2017.02.014](https://doi.org/10.1016/J.JCP.2017.02.014).

- Dickson, Andrew N., James N. Barry, Kevin A. McDonnell, and Denis P. Dowling. 2017. "Fabrication of Continuous Carbon, Glass and Kevlar Fibre Reinforced Polymer Composites Using Additive Manufacturing." *Additive Manufacturing* 16 (August): 146–152. doi:[10.1016/j.addma.2017.06.004](https://doi.org/10.1016/j.addma.2017.06.004).
- Ehsani, Amir, and Hamid Dalir. 2019. "Multi-Objective Optimization of Composite Angle Grid Plates for Maximum Buckling Load and Minimum Weight Using Genetic Algorithms and Neural Networks." *Composite Structures* 229 (December): 111450. doi:[10.1016/j.compstruct.2019.111450](https://doi.org/10.1016/j.compstruct.2019.111450).
- Fang, Guoxin, Tianyu Zhang, Sikai Zhong, Xiangjia Chen, Zichun Zhong, and Charlie C.L. Wang. 2020. "Reinforced FDM." *ACM Transactions on Graphics* 39 (6), doi:[10.1145/3414685.3417834](https://doi.org/10.1145/3414685.3417834).
- Gibson, Brian T., Paritosh Mhatre, Michael C. Borish, Celeste E. Atkins, John T. Potter, Joshua E. Vaughan, and Lonnie J. Love. 2022. "Controls and Process Planning Strategies for 5-Axis Laser Directed Energy Deposition of Ti-6Al-4V Using an 8-Axis Industrial Robot and Rotary Motion." *Additive Manufacturing* 58 (October): 103048. doi:[10.1016/j.addma.2022.103048](https://doi.org/10.1016/j.addma.2022.103048).
- Goh, Guo Dong, Song Jiang Casper Neo, Vishwesh Dikshit, and Wai Yee Yeong. 2022. "Quasi-Static Indentation and Sound-Absorbing Properties of 3D Printed Sandwich Core Panels." *Journal of Sandwich Structures & Materials* 24 (2): 1206–1225. doi:[10.1177/10996362211037015](https://doi.org/10.1177/10996362211037015).
- Goh, G. D., V. Dikshit, A. P. Nagalingam, G. L. Goh, S. Agarwala, S. L. Sing, J. Wei, and W. Y. Yeong. 2018. "Characterization of Mechanical Properties and Fracture Mode of Additively Manufactured Carbon Fiber and Glass Fiber Reinforced Thermoplastics." *Materials & Design* 137 (January): 79–89. doi:[10.1016/j.matdes.2017.10.021](https://doi.org/10.1016/j.matdes.2017.10.021).
- Goh, Guo Liang, Haining Zhang, Tzyy Haur Chong, and Wai Yee Yeong. 2021. "3D Printing of Multilayered and Multimaterial Electronics: A Review." *Advanced Electronic Materials* 7 (10): 2100445. doi:[10.1002aelm.202100445](https://doi.org/10.1002aelm.202100445).
- Gu, David Xianfeng, Feng Luo, and Shing Tung Yau. 2010. "Fundamentals of Computational Conformal Geometry." *Mathematics in Computer Science* 4 (4): 389–429. doi:[10.1007/S11786-011-0065-6](https://doi.org/10.1007/S11786-011-0065-6).
- Gu, Xianfeng, Yalin Wang, Tony F. Chan, Paul M. Thompson, and Shing Tung Yau. 2004. "Genus Zero Surface Conformal Mapping and Its Application to Brain Surface Mapping." *IEEE Transactions on Medical Imaging* 23 (8): 949–958. doi:[10.1109/TMI.2004.831226](https://doi.org/10.1109/TMI.2004.831226).
- Gu, Xianfeng David, Wei Zeng, Feng Luo, and Shing Tung Yau. 2012. "Numerical Computation of Surface Conformal Mappings." *Computational Methods and Function Theory* 11 (2): 747–787. doi:[10.1007/BF03321885](https://doi.org/10.1007/BF03321885).
- Hou, Zhanghao, Xiaoyong Tian, Ziqi Zheng, Junkang Zhang, Lu Zhe, Dichen Li, Andrei V. Malakhov, and Alexander N. Polilov. 2020. "A Constitutive Model for 3D Printed Continuous Fiber Reinforced Composite Structures with Variable Fiber Content." *Composites Part B: Engineering* 189 (May): 107893. doi:[10.1016/J.COMPOSITESB.2020.107893](https://doi.org/10.1016/J.COMPOSITESB.2020.107893).
- Jiang, Caigui, Kaust Cheng Wang, Kaust Florian Rist, Tu Wien Johannes Wallner, Tu Graz, Cheng Wang, Florian Rist, Tu Wien, Johannes Wallner, and Helmut Pottmann. 2020. "Quad-Mesh Based Isometric Mappings and Developable Surfaces." *ACM Transactions on Graphics* 39 (4): 13. doi:[10.1145/3386569.3392430](https://doi.org/10.1145/3386569.3392430).
- Jiang, Jingchao, Xun Xu, and Jonathan Stringer. 2019. "Optimisation of Multi-Part Production in Additive Manufacturing for Reducing Support Waste." *Virtual and Physical Prototyping* 14 (3): 219–228. doi:[10.1080/17452759.2019.1585555](https://doi.org/10.1080/17452759.2019.1585555).
- Jin, Miao, Xianfeng Gu, Ying He and Yalin Wang. 2022. "Conformal Geometry Computational Algorithms and Engineering Applications." Accessed September 4.
- Khamayseh, Ahmed, and C. Wayne Mastin. 1996. "Computational Conformal Mapping for Surface Grid Generation." *Journal of Computational Physics* 123 (2): 394–401. doi:[10.1006/jcph.1996.0032](https://doi.org/10.1006/jcph.1996.0032).
- Konaković, Mina, Keenan Crane, Bailin Deng, Sofien Bouaziz, Daniel Piker, and Mark Pauly. 2016. "Beyond Developable." *ACM Transactions on Graphics* 35 (4), doi:[10.1145/2897824.2925944](https://doi.org/10.1145/2897824.2925944).
- Kubalak, Joseph R., Alfred L. Wicks, and Christopher B. Williams. 2018. "Using Multi-Axis Material Extrusion to Improve Mechanical Properties Through Surface Reinforcement." *Virtual and Physical Prototyping* 13 (1): 32–38. doi:[10.1080/17452759.2017.1392686](https://doi.org/10.1080/17452759.2017.1392686).
- Liang, Fusheng, Chengwei Kang, and Fengzhou Fang. 2020. "A Smooth Tool Path Planning Method on NURBS Surface Based on the Shortest Boundary Geodesic Map." *Journal of Manufacturing Processes* 58 (October): 646–658. doi:[10.1016/j.jmapro.2020.08.047](https://doi.org/10.1016/j.jmapro.2020.08.047).
- Lingappan, Niranjanmurthi, Sungmook Lim, Guk Hwan Lee, Huynh Thanh Tung, Van Hoang Luan, and Wonoh Lee. 2022. "Recent Advances on Fiber-Reinforced Multifunctional Composites for Structural Supercapacitors." *Functional Composites and Structures* 4 (1): 012001. doi:[10.1088/2631-6331/ac4de9](https://doi.org/10.1088/2631-6331/ac4de9).
- Liu, Guang, Yi Xiong, and Limin Zhou. 2021. "Additive Manufacturing of Continuous Fiber Reinforced Polymer Composites: Design Opportunities and Novel Applications." *Composites Communications* 27 (October): 100907. doi:[10.1016/J.COCO.2021.100907](https://doi.org/10.1016/J.COCO.2021.100907).
- Maes, Vincent K., Leonid Pavlov, and Sahak M.(Samo) Simonian. 2019. "An Efficient Semi-Automated Optimisation Approach for (Grid-Stiffened) Composite Structures: Application to Ariane 6 Interstage." *Composite Structures* 209 (February): 1042–1049. doi:[10.1016/j.compstruct.2016.02.082](https://doi.org/10.1016/j.compstruct.2016.02.082).
- Matsuzaki, Ryosuke, Masahito Ueda, Masaki Namiki, Tae Kun Jeong, Hirosuke Asahara, Keisuke Horiguchi, Taishi Nakamura, Akira Todoroki, and Yoshiyasu Hirano. 2016. "Three-Dimensional Printing of Continuous-Fiber Composites by in-Nozzle Impregnation." *Scientific Reports* 6 (1): 1–7. doi:[10.1038/srep23058](https://doi.org/10.1038/srep23058).
- Naranjo-Lozada, Juan, Horacio Ahuett-Garza, Pedro Orta-Castañón, Wilco M.H. Verbeeten, and Daniel Sáiz-González. 2019. "Tensile Properties and Failure Behavior of Chopped and Continuous Carbon Fiber Composites Produced by Additive Manufacturing." *Additive Manufacturing* 26 (March): 227–241. doi:[10.1016/j.addma.2018.12.020](https://doi.org/10.1016/j.addma.2018.12.020).
- Nault, Isaac M., Gehn D. Ferguson, and Aaron T. Nardi. 2021. "Multi-Axis Tool Path Optimization and Deposition Modeling for Cold Spray Additive Manufacturing." *Additive Manufacturing* 38 (February): 101779. doi:[10.1016/j.addma.2020.101779](https://doi.org/10.1016/j.addma.2020.101779).

- Nelson, Todd G., Trent K. Zimmerman, Spencer P. Magleby, Robert J. Lang, and Larry L. Howell. 2019. "Developable Mechanisms on Developable Surfaces." *Science Robotics* 4 (27), doi:10.1126/SCIROBOTICS.AAU5171/SUPPL_FILE/AAU5171_SM.PDF.
- Nuh, Mishael, Robin Oval, John Orr, and Paul Shepherd. 2022. "Digital Fabrication of Ribbed Concrete Shells Using Automated Robotic Concrete Spraying." *Additive Manufacturing* 59 (November): 103159. doi:10.1016/j.addma.2022.103159.
- Parandoush, Pedram, Levi Tucker, Chi Zhou, and Dong Lin. 2017. "Laser Assisted Additive Manufacturing of Continuous Fiber Reinforced Thermoplastic Composites." *Materials & Design* 131 (October): 186–195. doi:10.1016/j.matdes.2017.06.013.
- Parker, M., A. Inthavong, E. Law, S. Waddell, N. Ezeokeke, R. Matsuzaki, and D. Arola. 2022. "3D Printing of Continuous Carbon Fiber Reinforced Polyphenylene Sulfide: Exploring Printability and Importance of Fiber Volume Fraction." *Additive Manufacturing* 54 (June): 102763. doi:10.1016/j.addma.2022.102763.
- Pedersen, David Bue, Eyþór Rúnar Eiríksson, Hans Nørgaard Hansen, and Jakob Skov Nielsen. 2016. "A Self-Calibrating Robot Based upon a Virtual Machine Model of Parallel Kinematics." *Virtual and Physical Prototyping* 11 (3): 227–234. doi:10.1080/17452759.2016.1208363.
- Qiao, Jing, Yingrui Li, and Longqiu Li. 2019. "Ultrasound-Assisted 3D Printing of Continuous Fiber-Reinforced Thermoplastic (FRTP) Composites." *Additive Manufacturing* 30 (December): 100926. doi:10.1016/j.addma.2019.100926.
- Shembekar, Aniruddha v, Yeo Jung Yoon, Alec Kanyuck, and Satyandra K. Gupta. 2019. "Generating Robot Trajectories for Conformal Three-Dimensional Printing Using Nonplanar Layers." *Journal of Computing and Information Science in Engineering* 19 (3), doi:10.1115/1.4043013/726284.
- Sieberer, Stefan, Chethan Savandaiah, Jürgen Leßlhummer, and Martin Schagerl. 2022. "Shear Property Measurement of Additively Manufactured Continuous Fibre Reinforced Plastics by In-Plane Torsion Testing." *Additive Manufacturing* 55 (July): 102805. doi:10.1016/j.addma.2022.102805.
- Suzuki, Takuya, Shinya Fukushige, and Mitsuyoshi Tsunori. 2020. "Load Path Visualization and Fiber Trajectory Optimization for Additive Manufacturing of Composites." *Additive Manufacturing* 31 (January): 100942. doi:10.1016/j.addma.2019.100942.
- Tan, Wen See, Muhammad Aidil bin Juhari, Qian Shi, Shengyang Chen, Domenico Campolo, and Juha Song. 2020. "Development of a New Additive Manufacturing Platform for Direct Freeform 3D Printing of Intrinsically Curved Flexible Membranes." *Additive Manufacturing* 36 (December): 101563. doi:10.1016/j.addma.2020.101563.
- Totaro, G., P. Spena, G. Giusto, F. de Nicola, S. Kiryenko, and S. Das. 2021. "Highly Efficient CFRP Anisogrid Lattice Structures for Central Tubes of Medium-Class Satellites: Design, Manufacturing, and Performance." *Composite Structures* 258 (February): 113368. doi:10.1016/j.compstruct.2020.113368.
- van de Werken, Nekoda, Pratik Koirala, Jafar Ghorbani, Derek Doyle, and Mehran Tehrani. 2021. "Investigating the Hot Isostatic Pressing of an Additively Manufactured Continuous Carbon Fiber Reinforced PEEK Composite." *Additive Manufacturing* 37 (January): 101634. doi:10.1016/j.addma.2020.101634.
- van de Werken, Nekoda, Halil Tekinalp, Pouria Khanbolouki, Soydan Ozcan, Andrew Williams, and Mehran Tehrani. 2020. "Additively Manufactured Carbon Fiber-Reinforced Composites: State of the Art and Perspective." *Additive Manufacturing* 31 (January): 100962. doi:10.1016/j.addma.2019.100962.
- Vasiliev, V. V., V. A. Barynin, and A. F. Razin. 2012. "Anisogrid Composite Lattice Structures – Development and Aerospace Applications." *Composite Structures* 94 (3): 1117–1127. doi:10.1016/j.compstruct.2011.10.023.
- Wang, Hao, Jie Tao, Kai Jin, Xiaoyue Wang, and Ying Dong. 2022. "Multifunctional Pressure/Temperature/Bending Sensor Made of Carbon Fibre-Multiwall Carbon Nanotubes for Artificial Electronic Application." *Composites Part A: Applied Science and Manufacturing* 154 (March): 106796. doi:10.1016/j.compositesa.2021.106796.
- Wang, Yaohui, Guoquan Zhang, Huilin Ren, Guang Liu, and Yi Xiong. 2022. "Fabrication Strategy for Joints in 3D Printed Continuous Fiber Reinforced Composite Lattice Structures." *Composites Communications* 30 (February): 101080. doi:10.1016/j.coco.2022.101080.
- Xiong, Yi, Sang In Park, Suhasini Padmanathan, Audelia Gumarus Dharmawan, Shaohui Foong, David William Rosen, and Gim Song Soh. 2019. "Process Planning for Adaptive Contour Parallel Toolpath in Additive Manufacturing with Variable Bead Width." *The International Journal of Advanced Manufacturing Technology* 105 (10): 4159–4170. doi:10.1007/s00170-019-03954-1.
- Xu, Ke, Yingguang Li, Lufeng Chen, and Kai Tang. 2019. "Curved Layer Based Process Planning for Multi-Axis Volume Printing of Freeform Parts." *Computer-Aided Design* 114 (September): 51–63. doi:10.1016/j.cad.2019.05.007.
- Zeng, Chengjun, Liwu Liu, Wenfeng Bian, Jinsong Leng, and Yanju Liu. 2021. "Compression Behavior and Energy Absorption of 3D Printed Continuous Fiber Reinforced Composite Honeycomb Structures with Shape Memory Effects." *Additive Manufacturing* 38 (February): 101842. doi:10.1016/j.addma.2021.101842.
- Zhang, Zhongsen, Yu Long, Zhe Yang, Kunkun Fu, and Yan Li. 2022. "An Investigation Into Printing Pressure of 3D Printed Continuous Carbon Fiber Reinforced Composites." *Composites Part A: Applied Science and Manufacturing* 162 (November): 107162. doi:10.1016/j.compositesa.2022.107162.
- Zhang, Guoquan, Yaohui Wang, Jian He, and Yi Xiong. 2023. "A Graph-Based Path Planning Method for Additive Manufacturing of Continuous Fiber-Reinforced Planar Thin-Walled Cellular Structures." *Rapid Prototyping Journal*, 29 (2): 344–353. doi:10.1108/RPJ-01-2022-0027/FULL/XML.
- Zhang, Guoquan, Yaohui Wang, Wanglin Qiu, Ke Dong, and Yi Xiong. 2022. "Geometric Characteristics of Single Bead Fabricated by Continuous Fiber Reinforced Polymer Composite Additive Manufacturing." *Materials Today: Proceedings* 70. doi:10.1016/j.mattod.2022.09.361.
- Zhao, Donghua, and Weizhong Guo. 2020. "Shape and Performance Controlled Advanced Design for Additive Manufacturing: A Review of Slicing and Path Planning." *Journal of Manufacturing Science and Engineering*,

Transactions of the ASME 142 (1), doi:10.1115/1.4045055/1046939.

Zhou, Ying, Liang Gao, and Hao Li. 2022. "Graded Infill Design Within Free-Form Surfaces by Conformal Mapping." *International Journal of Mechanical Sciences* 224 (June): 107307. doi:10.1016/j.ijmecsci.2022.107307.

Zolfagharian, Ali, M. A. Parvez Mahmud, Saleh Gharaie, Mahdi Bodaghi, Abbas Z. Kouzani, and Akif Kaynak. 2020. "3D/4D-Printed Bending-Type Soft Pneumatic Actuators: Fabrication, Modelling, and Control." *Virtual and Physical Prototyping* 15 (4): 373–402. doi:10.1080/17452759.2020.1795209.

Appendix A

The working conical surface and mapping plane are parameterised as:

$$\begin{aligned} \mathbf{s}_1 &= (1-v) \begin{bmatrix} r_1 \cos u \\ r_1 \sin u \\ z_1 \end{bmatrix} + v \begin{bmatrix} r_2 \cos u \\ r_2 \sin u \\ z_2 \end{bmatrix}, \quad v \in [0, 1], \quad u \\ &\in [0, 2\pi], \end{aligned} \quad (A1)$$

$$\mathbf{s}_2 = \begin{bmatrix} x \\ y \\ z \end{bmatrix}, \quad (A2)$$

where r_1 , r_2 , z_1 , and z_2 are constants. The first fundamental forms of the conical surface and plane are:

$$ds_1^2 = ((1-v)r_1 + vr_2)^2 d_u^2 + ((r_2 - r_1)^2 + (z_2 - z_1)^2) d_v^2, \quad (A3)$$

$$ds_2^2 = dx^2 + dy^2. \quad (A4)$$

The conformal mapping function $f(u, v)$ is:

$$\begin{bmatrix} x \\ y \\ z \end{bmatrix} = \begin{bmatrix} \frac{u}{\sqrt{(r_2 - r_1)^2 + (z_2 - z_1)^2}} \ln \frac{(r_2 - r_1)v + r_1}{r_1} \\ 0 \\ 0 \end{bmatrix}. \quad (A5)$$

The inverse operator of conformal mapping $f^{-1}(x, y, z)$ is:

$$\begin{bmatrix} u \\ v \end{bmatrix} = \begin{bmatrix} \frac{x}{r_1} \left(e^{\frac{(r_2 - r_1)y}{\sqrt{(r_2 - r_1)^2 + (z_2 - z_1)^2}}} - 1 \right) \\ \frac{y}{r_2 - r_1} \end{bmatrix}. \quad (A6)$$

The isometric mapping function $g(u, v)$ is:

$$\begin{bmatrix} x \\ y \\ z \end{bmatrix} = \begin{bmatrix} \sqrt{1 + \frac{(z_2 - z_1)^2}{(r_2 - r_1)^2}} (r_1 + (r_2 - r_1)v) \cos \frac{u}{\sqrt{1 + \frac{(z_2 - z_1)^2}{(r_2 - r_1)^2}}} \\ \sqrt{1 + \frac{(z_2 - z_1)^2}{(r_2 - r_1)^2}} (r_1 + (r_2 - r_1)v) \sin \frac{u}{\sqrt{1 + \frac{(z_2 - z_1)^2}{(r_2 - r_1)^2}}} \\ 0 \end{bmatrix}. \quad (A7)$$

The inverse operator of conformal mapping $g^{-1}(x, y, z)$ is:

$$\begin{bmatrix} u \\ v \end{bmatrix} = \begin{bmatrix} \sqrt{1 + \frac{(z_2 - z_1)^2}{(r_2 - r_1)^2}} \cos^{-1} \frac{x}{\sqrt{x^2 + y^2}} \\ \frac{\sqrt{(x^2 + y^2)(r_2 - r_1)^2}}{r_2 - r_1} - r_1 \end{bmatrix}. \quad (A8)$$